Morphological and crystallographic features of α' martensite in binary Ti–Hf alloy

M. Matsuda [a,*], S. Ohsumi [b], S. Ii [c]

[a] *Division of Materials Science and Chemistry, Faculty of Advanced Science and Technology, Kumamoto University, 2-39-1 Kurokami, Kumamoto 860-8555, Japan*
[b] *Department of Materials Science and Engineering, Kumamoto University, 2-39-1 Kurokami, Kumamoto 860-8555, Japan*
[c] *Research Center for Structural Materials, National Institute for Materials Science (NIMS), 1-2-1 Sengen, Tsukuba 305-0047, Japan*

* Corresponding author. Tel.: +81 96 342 3718; fax: +81 96 342 3710.
E-mail address: matsuda@alpha.msre.kumamoto-u.ac.jp (M. Matsuda).

Abstract We investigated the morphological and crystallographic features of α' martensite variants in Ti-25 at% Hf and Ti-50 at% Hf alloys by transmission Kikuchi diffraction and transmission electron microscopy. On the basis of the results, we also discussed the formation process of variants and the self-accommodation. Both alloys, after solution-treatment and quenching in ice water, consisted of α' martensite with a hexagonal close-packed structure. The α' martensite exhibited a larger plate-like morphology several micrometers in length, along with a finer morphology with a width of tens of nanometers. The formation of $\{10\bar{1}1\}_{\alpha'}$ twins was induced within a larger correspondence variant (CV) as a lattice-invariant shear (LIS), and $\{10\bar{1}1\}_{\alpha'}$ twins were also the boundaries bounded two neighboring CVs. In formation process of the martensite variants of Ti–Hf alloys, a larger CV with a plate-like morphology is first formed with a $\{10\bar{1}1\}_{\alpha'}$ twin as an LIS in a β parent phase; finer CVs are subsequently generated from the step-like boundary with the $\{10\bar{1}1\}_{\alpha'}$ twin plane, followed by the formation of a pair of CVs with the twin plane to relax the transformation strain.

Keywords Ti-Hf alloy, Thermoelastic martensitic transformation, Self-accommodation, twin, Transmission Kikuchi diffraction, Transmission electron microscopy

Introduction

Thermoelastic martensitic transformation plays an important role in shape-memory effects and superelasticity [1]. The microstructure of thermoelastic martensite is characterized by the combination of multiple variants, which reduce the elastic strain energy via transformation; this phenomenon is known as self-accommodation. The self-accommodation mechanism of various alloys has been extensively studied [2-5]. For example, the self-accommodation morphologies of near-equiatomic TiNi alloys, which undergo the thermoelastic martensitic transformation from the B2 parent phase to the B19' structure, have been reported [6,7]. Because of the V-shaped minimum unit consisting of two habit plane variants (HPVs) connected to form a $\{\bar{1}\bar{1}\,1\}_{B19'}$ Type I variant accommodation twin, the hexangular morphology consisting of six HPVs is ideally suited for self-accommodation. Among binary Ti-based alloys that undergo a thermoelastic martensitic transformation, Ti–Mo [8,9], Ti–Nb [10,11], and Ti–V [12,13] alloys consist of a disordered body-centered cubic (bcc) structure as the parent phase. Ti–Zr alloys, which are composed of two elements of the same group in the periodic table, have been reported to exhibit shape-memory effects [14]. These alloys undergo a thermoelastic martensitic transformation from the β (bcc) structure to the α' (hexagonal close-packed, hcp) structure and have larger striped-like martensitic plates along with finer twin structures [9,14]. Their interface of martensitic variants is also composed of a $\{10\bar{1}1\}_{\alpha'}$ twin. In the Ti–Hf alloys, which also consisting of elements of the same periodic group, Ti and Hf form a complete solid-solution according to the Ti–Hf binary phase diagram [15]. The mechanical properties of Ti–Hf alloys have been investigated [16-18]. In addition, as-cast and furnace-cooled Ti–Hf alloys undergo a diffusional transformation from the β (bcc) and α (hcp) phases, whereas α' martensite with a hcp structure is formed via rapid quenching [19-21]. However, as far as we know, the martensite variants, internal defects, lattice invariant shear (LIS), and the self-accommodation mechanism of Ti–Hf alloys have not been clarified. Understanding the thermoelastic martensitic transformation by clarifying the LIS and self-accommodation is important because it will lead to the improvement of shape-memory properties and the development of new shape-memory alloys.

In the present study, we investigated the morphological and crystallographic features of α' martensite variants in the Ti-25 at% Hf alloy, which has a lower β transus at ~1073 K in the binary Ti–Hf phase diagram, and Ti-50 at% Hf alloy by transmission Kikuchi diffraction (TKD) [22] and transmission electron microscopy (TEM). The formation process of α' martensite and the self-accommodation are discussed on the basis of the results.

Material and methods

Ti-25 at% Hf and Ti-50 at% Hf alloys (hereinafter referred as 25Hf and 50Hf, respectively) were prepared from 99.97 mass% Ti and 99.9 mass% Hf by arc melting under an Ar atmosphere. The 25Hf and 50Hf ingots were homogenized under an Ar atmosphere at 1273 K or 1473 K, respectively, for 36 ks. The samples with a prescribed shape were subsequently encapsulated in quartz ampoules under an Ar atmosphere and solution-treated at 1123 K, 1223 K, 1323 K, and 1523 K (above the β transus of each alloy) for 3.6 ks; after the solution treatment, the samples were quenched in ice water by breaking the ampoule and quenched by cooling in the furnace (hereinafter referred as water-quenched (WQ) and furnace-cooled (FC) samples, respectively).

The constituent phases of the alloys were examined by X-ray diffraction (XRD) using a Rigaku Ultima IV system equipped with a Cu Kα radiation source operated at 40 kV and 40 mA; samples were scanned at a step size of 0.02° and a scan speed of 1°/min. The lattice parameters of the α phase and α' martensite were refined on the basis of the XRD measurements; the refinement was conducted by the Pawley method [23] using the Rigaku PDXL2.4 software. The crystal orientation was determined by scanning electron microscopy (SEM) using an instrument (HITACHI High Tech. SU5000) equipped with a TKD detector and operated at an acceleration voltage of 20 kV. For TKD and TEM studies, 3 mm-diameter disks were spark-cut from the solution-treated specimens. These disks were electropolished at ~243 K using a twin-jet method in an electrolyte solution consisting of 20% H_2SO_4 and 80% CH_3OH by volume. In addition, martensite variants were analyzed by TKD on the basis of the lattice correspondence between the bcc and the hcp structures; that is, they were analyzed using the Burgers orientation relations (OR) $\{110\}_\beta$ // $(0001)_{\alpha'}$, $<111>_\beta$ // $<11\bar{2}0>_{\alpha'}$ [24]. TEM observations were carried out with a JEM-2100PLUS microscope (JEOL, Tokyo) operated at an accelerating voltage of 200 kV. In addition, martensite variants were analyzed by an automated crystal lattice orientation mapping (ACOM) method [25, 26] with a JEM-2800 microscope (JEOL, Tokyo).

Results

Crystal Structures and Lattice Parameters

Figure 1 shows the room-temperature XRD patterns of the 25Hf alloys solution-treated at 1223 K followed by furnace cooling and water quenching. These alloys consisted of the α and α' (hcp) phases (space group: $P6_3/mmc$). The 50Hf alloys solution-treated at 1523 K followed by furnace cooling and water quenching were also composed of α and α' phases. Here, the α and α' phases can be identified on the basis of the TKD and TEM analyses described later. No peak of the β phase or precipitate was present in the XRD patterns of the 25Hf alloy samples solution-treated at 1223 K. This lack of a β phase or precipitate indicates complete solid-solution formation according to the Ti–Hf binary phase diagram [15]. The lattice parameters and reliability of the fitting results for the α and α' phase for each specimen, which were refined using the Pawley method [23], are listed in Table 1. These results are in good agreement with data reported previously [27,28]. The lattice parameters of the 50Hf alloy are slightly larger than those of the 25Hf alloy because of the larger atomic radius of Hf compared with that of Ti [29].

Microstructure of FC and WC Ti–Hf Alloys

We conducted TEM observations to investigate the microstructure of the FC and WC Ti–Hf alloys. Figure 2(a) and (b) show the bright-field images of the FC 25Hf alloy solution-treated at 1223 K and the FC 50Hf alloy solution-treated at 1523 K, respectively. These samples consisted of granular α phase with a grain size of several micrometers, consistent with the results of a previous investigation [21]. Notably, no twins or fine plates were observed inside the grain of either alloy, suggesting that the α phase of the FC Ti–Hf alloys formed via a diffusion process. Figure 2(c) and (d) show the bright-field images of the WQ 25Hf alloy solution-treated at 1223 K and the WQ 50Hf alloy solution-treated at 1523 K, respectively. Numerous variants with fine plate-like morphology were observed. Therefore, the WQ Ti-Hf alloys are composed of the α' phase formed by martensitic transformation.

Figure 3(a) and (b) respectively show the image quality (IQ) map and an inverse pole figure (IPF) with a confidence index (CI) value greater than 0.1 for the α' phase in the WQ 25Hf alloy solution-treated at 1123 K, as obtained by TKD. The α' phase consisted of both a larger variant with a plate-like morphology several micrometers in length and the finer variants a few hundred nanometers in width. According to the lattice correspondence between the Burgers OR and considering the existence of two crystallographic equivalent variants of $<111>_\beta$ directions for each $\{110\}_\beta$ plane, the β parent phase is composed of 12 identifiable CVs denoted as CV1 to CV12 (Table 2). Figure 3(c) shows a variant map and (d) the area fraction of each CV based on the lattice correspondence, respectively. The results indicate that the larger plate-like variant

consisted of CV11–CV4 and that the finer variants were composed of coupling pairs of CVs with approximately equal volume fractions, such as CV6–CV8 and CV1–CV10, as indicated by the white arrows in Fig. 3(c). Trace analysis using the pole figures recorded on the $\{10\bar{1}1\}_{\alpha'}$ plane in the red rectangular-shaped area in Fig. 3(c) indicates that the variant interfaces (I) between CV11 and CV4 were composed of the $\{10\bar{1}1\}_{\alpha'}$ plane, meaning the $\{10\bar{1}1\}_{\alpha'}$ twin plane [19], as shown in Fig. 3(e). On the basis of these observations, the morphological and crystallographic features of the microstructure of WQ 25Hf alloy demonstrate that the α' phase can be characterized as the variants induced by the martensitic transformation. Figure 3(f) shows the grain reference orientation deviation (GROD) map corresponding to Fig. 3(c), providing the strain distribution [30]. This map indicates that the remarkable strain distribution was not observed at the interface between CVs or inside a single CV. The mechanism of strain relaxation during the martensitic transformation is discussed later.

In the bright-field image of the WQ 25Hf alloy solution-treated at 1123 K (Fig. 4(a)), the larger plate-like CV several micrometers in length and the finer CVs a few hundred nanometers in width are observed. The selected-area diffraction pattern (SADP) in Fig. 4(b), which corresponds to boundary B in Fig. 4(a), consists of two sets of reflections that are mirror-symmetrical with respect to the $(1\bar{1}0\bar{1})_{CV1}$// $(1\bar{1}01)_{CV10}$ plane viewed from the $[1\bar{2}13]_{CV1}$ and $[\bar{2}\bar{1}\bar{1}3]_{CV10}$ directions of the α' martensite. This result indicates that the boundary was a $\{10\bar{1}1\}_{\alpha'}$ twin interface. Also, boundary C in Fig. 4(a) was a $\{10\bar{1}1\}_{\alpha'}$ twin interface, as shown in the SADP in Fig. 4(c). Therefore, a pair of fine CVs were bounded by a $\{10\bar{1}1\}_{\alpha'}$ twin plane. Notably, the interface in the larger plate-like variant consists of step-like boundaries, as indicated by the white arrows in Fig. 4(a). The SADP in Fig. 4(d), which corresponds to area D in Fig. 4(a), was composed of $\{10\bar{1}1\}_{\alpha'}$ twin planes. This step-like boundary is described in the Discussion.

TEM-ACOM analysis was performed to investigate the finer plate-like CV in the WQ 50Hf alloy solution-treated at 1523 K in detail. Figure 5(a) and (b) shows the IQ map and IPF with a CI value greater than 0.1 for the α' phase, respectively, as acquired using TEM-ACOM analysis. The α' martensite variants consisted of a larger plate-like morphology several micrometers in length and finer ones tens of nanometers in width. Figure 5(c) shows a variant map and (d) the area fraction of each CV on the basis of the lattice correspondence in Table 2, respectively. These results indicate that the larger plate-like variant was composed of CV5–CV7 and that the finer variants were composed mainly of CV2–CV3 and CV1–CV5 coupling pairs, as indicated by the white arrows in Fig. 5(c). The strain distribution interface between each CV and inside a single CV was not large, as shown in the GROD map in Fig. 5(e).

Figure 6(a) and (b) shows the IQ map and IPF with a CI value greater than 0.1 for α'

martensite, as obtained by TEM-ACOM analysis of another area of the WQ 50Hf alloy. This analysis shows the triangular-like morphology with a combination of CV plates several hundred nanometers in width. CV coupling pairs such as CV4–CV7 and CV1–CV11 were also observed, as indicated by the variant map and the area fraction of each CV in Fig. 6(c) and (d), respectively. The GROD map in Fig. 6(e) indicates that the strain distribution interface between each CV and inside a single CV was not large except for the area where each variant should collide, as indicated by the white arrows.

Figure 7(a) shows a bright-field image of the microstructure of the WQ 50Hf alloy solution-treated at 1323 K. Variants with a triangle-like morphology were observed, and few lattice defects were observed inside these variants. Figure 7(b) and (c) shows the SADPs of boundaries B and C in Fig. 7(a), respectively. These results indicate that the boundaries consisted of $\{10\bar{1}1\}_{\alpha'}$ twins. Notably, step-like boundaries similar to the boundaries of the larger CV in Fig. 4(a) were observed, as indicated by the yellow arrows in Fig. 7(a). Also, fine variants existed inside one large variant, as indicated by the yellow arrow in Fig. 7(d). The SADP in Fig. 7(e), which corresponds to area E in Fig. 7(d), indicates a $\{10\bar{1}1\}_{\alpha'}$ twin pattern. Judging from the morphologies and crystallographic features of these twins, they should be an LIS. Also, $\{13\bar{4}1\}_{\alpha'}$ twins existed at the boundaries of CVs, as shown in the bright-field image and SADP corresponding to boundary G in Fig. 7(f).

Discussion

On the basis of the present observation results, the morphological and crystallographic features of WQ 25Hf and WQ 50Hf alloys are almost the same. Therefore, we first discuss the lattice strain accompanying the martensitic transformation. The lattice distortion was calculated using the lattice parameters for each structure of both alloys. Here, the lattice parameters for the β parent phase should be strictly estimated from XRD measurements conducted at temperatures greater than the reverse martensitic transformation point. However, the Hf in the alloys tended to oxidize and easily form Hf-oxide. Therefore, we used reference values to estimate the lattice parameters of each β parent phase on the basis of Vegard's law [31] for a complete solid solution between Ti [32] and Hf [33] elements and that of TiHf alloy [28]. The lattice distortion was calculated on the basis of the Pitsch–Schrader orientation relationship [34, 35], as follows. For the WQ 25Hf alloy,

$\boldsymbol{\eta}_1 = c_{\mathrm{hcp}} / \sqrt{2}a_{\mathrm{bcc}} = 1.018 \simeq 1$

$\boldsymbol{\eta}_2 = \sqrt{3}a_{\mathrm{hcp}} / \sqrt{2}a_{\mathrm{bcc}} = 1.120 > 1$

$\boldsymbol{\eta}_3 = a_{\mathrm{hcp}} / a_{\mathrm{bcc}} = 0.914 < 1$

where a_{bcc} is the lattice parameter of the β phase and a_{hcp} and c_{hcp} are the lattice parameters of the α' phase. For the WQ 50Hf alloy,

$\eta_1 = 1.016 \simeq 1$

$\eta_2 = 1.114 > 1$

$\eta_3 = 0.910 < 1$

No substantial difference was observed between the lattice distortion of each alloy. Therefore, we concluded that the fundamental features of CVs for each alloy are nearly identical.

We here discuss the formation process of martensite variants and self-accommodation to relax the transformation strain. In the early stage of martensitic transformation, a larger CV with a plate-like morphology is formed, introducing the $\{10\bar{1}1\}_{\alpha'}$ twin as an LIS. The interface of a larger CV consisted of step-like morphologies (Fig. 4). These step-like boundaries have a $\{10\bar{1}1\}_{\alpha'}$ twin relationship for other CVs. Concerning the OR and combination of CVs, each $(0001)_{\alpha'}$ basal plane of CV1 and CV2 is common for the $(110)_{\beta}$ plane of the β phase, and each a-axis has a rotational relationship. In addition, CV1(2) has a $\{10\bar{1}1\}_{\alpha'}$ twin relationship for (a) CV3(4), (b) CV5(6), (c) CV9(10), and (d) CV11(12), respectively, whereas a $\{10\bar{1}2\}_{\alpha'}$ twin relationship exists between CV1(2) and CV7(8), as shown in the gray-hatched area of Fig. 8. Formation of the $\{10\bar{1}2\}_{\alpha'}$ twin is frequently induced by deformation in pure Ti and Ti-based alloys [36,37]. However, no $\{10\bar{1}2\}_{\alpha'}$ twin is induced in the present Ti–Hf alloys; that is, no combination of CVs bounded by an $\{10\bar{1}2\}_{\alpha'}$ twin was observed in the Ti–Hf alloys. The origin of this behavior can be explained on the basis of twinning shear S. The magnitude of S of a $\{10\bar{1}1\}_{\alpha'}$ twin is smaller than that of a $\{10\bar{1}2\}_{\alpha'}$ twin, as deduced from the c/a ratio of the lattice parameters [38,39], indicating that a $\{10\bar{1}1\}_{\alpha'}$ twin is more likely to form than a $\{10\bar{1}2\}_{\alpha'}$ twin (Table 3). However, the $\{13\bar{4}1\}_{\alpha'}$ twin shown in Fig. 7(g,h) was observed even though the magnitude of S for the $\{13\bar{4}1\}_{\alpha'}$ twin is larger than that of $\{10\bar{1}2\}_{\alpha'}$ twin. Therefore, an alternative origin of twin formation is related to martensitic transformation in the bcc-based alloy. It is well known that $\{110\}_{bcc}$ planes shear in the $<1\bar{1}0>_{bcc}$ directions [1]. That is, the $\{0001\}_{hcp}$ basal plane becomes a shear plane, suggesting that the transformation strain would accumulate on the $\{0001\}_{hcp}$ basal plane. In the case of a $\{10\bar{1}2\}_{\alpha'}$ twin, for example, the basal plane of CV1(2) is orthogonal to that of CV7(8). Thus, a combination of CVs with the $\{10\bar{1}2\}_{\alpha'}$ twin relationship could not easily relax the transformation strain accompanying the shear during the martensitic transformation. Therefore, pairs of CVs bounded by a $\{10\bar{1}1\}_{\alpha'}$ twin are more common in the present Ti–Hf alloys. In addition, these observations are in agreement with the slight strain distribution at the interface between CVs, as shown in the results of Fig. 3(f) and Fig. 5(e). Consequently, the finer CVs would be generated from the interfaces of the larger CV with

a step-like boundary to relax the transformation strain; that is, the step-like boundary is considered to not be an impinged CV interface but the formation site of a CV. Similarly, the triangular-shaped CVs bounded by a $\{10\bar{1}1\}_{\alpha'}$ twin would first form and the finer twins would be generated from the step-like boundaries, as indicated by the yellow arrows in Fig. 7(a). Here, no twin exists within each finer CV, including the triangular-shaped one. According to the phenomenological theory of martensite crystallography, under the conditions where $\boldsymbol{\eta}_1$ is approximately 1 and $\boldsymbol{\eta}_2$ and $\boldsymbol{\eta}_3$ are greater than and less than 1, respectively, no transformation twin within one CV is required to relax the strain during martensitic transformation [40,41]. Therefore, the finer CVs smaller than approximately 1 μm, including the triangular-shaped CVs, would not have an LIS except for the larger CV several micrometers in length. This finding suggests that the finer CVs accommodate the transformation strain by forming a pair of CVs bounded by a $\{10\bar{1}1\}_{\alpha'}$ twin. Consequently, in the formation process of martensite variants shown in Fig. 9, a larger CV with a plate-like morphology is first formed with a $\{10\bar{1}1\}_{\alpha'}$ twin (i) as an LIS in a β parent phase; the finer twins (ii) bounded by a $\{10\bar{1}1\}_{\alpha'}$ twin are then generated from the step-like boundary, followed by the formation of twin (iii) to relax the transformation strain as a CV pair with twin (ii). The volume fraction and distribution of the larger and triangular-like CVs likely depend on the grain size of the bcc parent phase and the heat-treatment conditions [42], which our group is currently studying.

Summary

We investigated the morphological and crystallographic features of α' martensite variants in Ti-25 at% Hf and Ti-50 at% Hf alloys by TKD and TEM. The formation process of α' martensite and the self-accommodation were also discussed on the basis of the results, which are summarized as follows:

1. Ti-25 at% Hf and Ti-50 at% Hf alloys solution-treated and then cooled in the furnace were composed of granular α (hcp) phase grains of several micrometers, formed by a diffusion process. Both solution-treated alloys, after quenching in ice water, consisted of α' martensite. Their lattice parameters were refined as follows:

Ti-25 at% Hf alloy; α: a = 0.303 nm, c = 0.478 nm, α': a = 0.304 nm, c = 0.480 nm

Ti-50 at% Hf alloy: α: a = 0.310 nm, c = 0.490 nm, α': a = 0.311 nm, c = 0.490 nm

2. The α' martensite was composed of a larger plate-like morphology several micrometers in length and a finer one tens of nanometers in width. The formation of $\{10\bar{1}1\}_{\alpha'}$ twins was induced within a CV as an LIS. The $\{10\bar{1}1\}_{\alpha'}$ twins were also the boundaries bounded by two neighboring CVs.

3. In the formation process of martensite variants of the Ti–Hf alloys, a larger CV with a plate-like morphology is first formed with a $\{10\bar{1}1\}_{\alpha'}$ twin as an LIS in a β parent phase and the finer CVs are generated from the step-like boundary with a $\{10\bar{1}1\}_{\alpha'}$ twin plane, followed by the formation of a pair of CVs with a $\{10\,\bar{1}\,1\}_{\alpha'}$ twin to relax the transformation strain. This mechanism indicates that the WQ-TiHf alloys have a typical feature of thermoelastic martensitic transformation.

Acknowledgments This work was supported by JSPS KAKENHI Grant Number JP23KK0087.

References

1. Otsuka, K., Wayman, C.M: Shape Memory Materials. Cambridge University Press, Cambridge, UK (1998)
2. Chakravorty, S., Wayman, C.M.: The thermoelastic martensitic transformation in β' Ni-Al alloys: I. Crystallography and morphology. Metall Trans A. (1976) doi:10.1007/BF02643970
3. Saburi, T., Wayman, C.M.: Crystallographic similarities in shape memory martensites. Acta Metall. (1979) doi:10.1016/0001-6160(79)90186-X
4. Adachi, K., Perkins, J., Wayman, C.M.: Type II twins in self-accommodating martensite plate variants in a Cu-Zn-Al shape memory alloy. Acta Metall. (1986) doi:10.1016/0001-6160(86)90150-1
5. Murakami, Y., Otsuka, K., Hanada, S., Watanabe, S.: Self-accommodation and morphology of 14M (7R) martensites in an Ni-37.0 at%Al alloy. Mater Sci Eng A. (1994) doi:10.1016/0921-5093(94)90415-4
6. Nishida, M., Nishiura, T., Kawano, H., Inamura, T.: Self-accommodation of B19' martensite in Ti-Ni shape memory alloys – Part I. Morphological and crystallographic studies of the variant selection rule. Philos Mag. (2012) doi:10.1080/14786435.2012.669858
7. Soejima, Y., Heima, H., Akamine, H., Inamura, T., Nishida, M.: Comparison of In Situ SEM and TEM observations of thermoelastic martensitic transformation in Ti–Ni shape memory alloy. Mater Trans. (2020) doi:10.2320/matertrans.MT-M2020219
8. Davis, R.: Martensitic transformations in Ti-Mo alloys. J Mater Sci. (1979) doi:10.1007/BF00772735
9. Sabeena, M., Murugesan, S., Anees, P., Mohandas, E., Vijayalakshmi. M.: Crystal

structure and bonding characteristics of transformation products of bcc b in Ti-Mo alloys. J Alloys Compd. (2017) doi:10.1016/j.jallcom.2016.12.155
10. Moffat, D.L., Larbalestier, D.C.: The competition between martensite and omega in quenched Ti-Nb alloys. Metall Trans A. (1988) doi:10.1007/BF02645135
11. Bönisch, M., Calin, M., Giebeler, L., Health, A., Annett, G., Skrotzki, W., Eckert, J.: Composition-dependent magnitude of atomic shuffles in Ti–Nb martensites. J Appl Crys.t (2014) doi:10.1107/S1600576714012576
12. Kuan, T.S., Ahrens, R.R., Sass, S.L.: The stress-induced omega phase transformation in Ti-V alloys. Metall Trans A. (1975) doi:10.1007/BF02642306
13. Aurelio, G., Guillermet, A.F., Cuello, G.J., Campo, J.: Metastable phases in the Ti-V system: Part I. Neutron diffraction study and assessment of structural properties. Metall Mater Trans A. (2002) doi:10.1007/s11661-002-0057-x
14. Li, Y., Cui, T., Zhang, F., Xu, H.: Shape memory behavior in Ti-Zr alloys. Scr Mater. (2011) doi:10.1016/j.scriptamat.2010.11.048
15. Bittermann, H., Rogl, P.: Critical assessment and thermodynamic calculation of the ternary system Boron-Hafnium-Titanium (B-Hf-Ti). J Phase Equilib. (1997) doi:10.1007/BF02646757
16. Imagram, A.G., Williams, D.N., Ogden, H.R.: Tensile properties of binary titanium-zirconium and titanium-hafnium alloys. J Less-Common Met. (1962) doi:10.1016/0022-5088(62)90068-1
17. Zhou, Y.L., Niinomi, M., Akabori, T.: Dynamic Young's modulus and mechanical properties of Ti-Hf alloys. Mater Trans. (2004) doi:10.2320/matertrans.45.1549
18. Sato, H., Kikuchi, M., Komatsu, M., Okuno, O., Okabe, T.: Mechanical properties of cast Ti-Hf alloy. J Biomed Mater Res. (2004) doi:10.1002/jbm.b.30169
19. Jayaraj, J., Ravi, K.R., Mallika, C., Mudali, U.K.: Microstructure and corrosion behavior of Hf-40 wt pct Ti alloy in nitic acid medium for reprocessing applications. Metall Mater Trans A. (2016) doi:10.1007/s11661-016-3602-8
20. Khlebnikova, Y.V., Rodionov, D.P., Suaridze, T.R., Egorova, L.Y., Kazantsev, V.A., Nikolaeva, N.V.: ESBD analysis of the structure of cast and quenched Hafnium-Titanium alloys. Phys Met Metallogr. (2018) doi:10.1134/S0031918X18090077
21. Khlebnikova, Y.V., Rodionov, D.P., Egorova, L.Y., Suaridze, T.R.: Crystallographic features of the α-phase structure in hafnium and hafnium-titanium alloys. Tech Phys. (2018) doi:10.1134/S106378421901016X
22. Sneddon, G.C., Trimby, P.W., Cairney, J.M.: Transmission Kikuchi diffraction in a scanning electron microscope: A review. Mater Sci Eng R. (2016) doi:10.1016/j.mser.2016.10.001
23. Pawley, G.S.: Unit-cell refinement from powder diffraction scans. J Appl Crystallogr.

(1981) doi:10.1107/S0021889881009618
24. Burgers, W.G.: On the process of transition of the cubic-body-centered modification into the hexagonal-close-packed modification of zirconium. Physica. (1934) doi:10.1016/S0031-8914(34)80244-3
25. Schwarzer, R.A.: Advances in crystal orientation mapping with the SEM and TEM. Ultramicroscopy (1997) doi:10.1016/S0304-3991(97)00010-7
26. Vincent, R., Midgley, P.A.: Double conical beam-rocking system for measurement of integrated electron diffraction intensities. Ultramicroscopy. (1994) https://doi.org/10.1016/0304-3991(94)90039-6
27. Kozhanov, V.N., Skripov, A.V., Romanov, E.P.: Hydrogen in $HfTi_2$ alloy: a formation of the hydrogen-stabilized $HfTi_2H_x$ phase with the C15-type host lattice. J Alloys Compd. (1998) doi:10.1016/S0925-8388(98)00132-7
28. Zhang, C.B., Li, W.D., Zhang, P., Wang, B.T.: Phase transition, elasticity, phonon spectra, and superconductive properties of equiatomic TiZr, TiHf, and ZrHf alloys at high pressure: Ab initio calculations. Comput Mater Sci. (2020) doi:10.1016/j.commatsci.2020.109637
29. Vainshtein, B.K., Fridkin, V.M., Indenbom, V.L.: Structure of Crystals, 3rd ed., Springer Verlag, Berlin (1995)
30. Zaefferer, S., Romano, P., Friedel, F.: EBSD as a tool to identify and quantify bainite and ferrite in low-alloyed Al-TRIP steels. J Microsc (Oxford, U.K.). (2008) doi:10.1111/j.1365-2818.2008.02010.x
31. Vegard, L.: The constitution of the mixed crystals and the filling of space of the atoms. Z. Phys. 5(1), 17–26 (1921)
32. Alekseyevskiy, N.Y., Ivanov, O.S., Rayevskiy. I.I., Stepanov, M.V.: Constitution diagram of the system niobium-titanium-zirconium and super conducting properties of the alloys. Phys. Met. Metallogr. 23, 1–28 (1967)
33. Ross, R.G., Hume, R.W.: High temperature X-ray metallography. I. A new Debye-Scherrer camera for use at very high temperatures. II. A new parafocusing camera. III. Applications to the study of chromium, hafnium, molybdenum, rhodium, ruthenium, and tungsten. J Less-Common Met. (1963) doi:10.1016/0022-5088(63)90031-6
34. Pitch, W., Schrader, A.: Die Ausscheidungsform des ε-Karbids im Ferrit und im Martensit beim Anlassen. Arch Elsenhuttenwesen. (1958) doi:10.1002/srin.195803018
35. Wang, S.C., Aindow, M., Starink, M.J.: Effect of self-accommodation on α/α boundary populations in pure titanium. Acta Mater. (2003) doi:10.1016/S1359-6454(03)00035-1
36. Xiao, L., Umakoshi, Y.: Orientation dependence of cyclic deformation behavior and dislocation structure in Ti-5at.% Al single crystals. Mater Sci Eng A. (2003)

doi:10.1016/S0921-5093(02)00104-1
37. Tirry, W., Bouvier, S., Benmhenni, N., Hammami, W., Habraken, A.M., Coghe, F., Schryvers, D., Rabet, L.: Twinning in pure Ti subjected to monotonic simple shear deformation. Mater Charact. (2012) doi:10.1016/j.matchar.2012.07.001
38. Yoo, M.H.: Slip, twinning, and fracture in hexagonal close-packed metals. Metall Trans A. (1981) doi:10.1007/BF02648537
39. Christian, J.W., Mahajan, S.: Deformation twinning. Prog Mater Sci. (1995) doi:10.1016/0079-6425(94)00007-7
40. Tadaki, T., Wayman, C.M.: Electron microscopy studies of martensitic transformations in $Ti_{50}Ni_{50-x}Cu_x$ alloys. Part II. Morphology and crystal structure of martensites. Metallography. (1982) doi:10.1016/0026-0800(82)90005-2
41. Delville, R., Kasinathan, S., Zhang, Z., Humbeeck, J.V., James, R.D., Schryvers, D.: Transmission electron microscopy study of phase compatibility in low hysteresis shape memory alloys. Philos Mag. (2010) doi:10.1080/14786430903074755
42. Nishida, M., Itai, I., Kitamura, K., Chiba, A., Yamauchi, K.: Effect of grain size of parent phase on twinning modes of B19' martensite in an equiatomic Ti-Ni shape memory alloy. J Phys IV. (1995) doi:10.1051/jp4/199558635

Figure Captions

Table 1 Lattice parameters and reliability of the fitting results for the α and α' phase for the Ti-25 at% Hf and Ti-50 at% Hf alloys solution-treated at 1223 K and 1523 K, respectively, followed by furnace cooling and water quenching, which were refined using the Pawley method.

Table 2 Lattice correspondence between the β parent phase and the α' martensite.

Table 3 Twinning shear of $\{10\bar{1}1\}_{\alpha'}$, $\{10\bar{1}2\}_{\alpha'}$ and $\{13\bar{4}1\}_{\alpha'}$ twins, based on the c/a ratio of the lattice parameters.

Fig. 1 Room-temperature XRD patterns of the Ti-25 at% Hf and Ti-50 at% Hf alloys solution-treated at 1223 K and 1523 K, respectively, followed by furnace cooling and water quenching.

Fig. 2 **a, b** Bright-field images of the Ti-25 at% Hf and Ti-50 at% Hf alloys solution-treated at 1223 K and 1523 K, respectively, followed by furnace cooling. **c, d** Bright-field images of the Ti-25 at% Hf and Ti-50 at% Hf alloys solution-treated at 1223 K and 1523 K, respectively, followed by water quenching.

Fig. 3 **a** Image quality map and **b** inverse pole figure with a confidence index value greater than 0.1 for the α' phase in the Ti-25 at% Hf alloy solution-treated at 1123 K followed by water quenching, respectively, as obtained by transmission Kikuchi diffraction. **c** Variant map and **d** area fraction of each CV based on the lattice correspondence, respectively. **e** Pole figure recorded on the $\{10\bar{1}1\}_{\alpha'}$ plane in the red rectangular-shaped area in **c**. **f** Grain reference orientation deviation map corresponding to **c**.

Fig. 4 **a** Bright-field image of the Ti-25 at% Hf alloy solution-treated at 1123 K followed by water quenching. **b, c, d** Selected-area diffraction patterns corresponding to boundaries B, C and D in **a**, respectively.

Fig. 5 **a** Image quality map and **b** inverse pole figure with a confidence index value greater than 0.1 for the α' phase in the Ti-50 at% Hf alloy solution-treated at 1523 K followed by water quenching, respectively, as acquired using transmission electron microscopy-automated crystal lattice orientation mapping analysis. **c** Variant map and **d**

area fraction of each CV based on the lattice correspondence, respectively. **e** Grain reference orientation deviation map corresponding to **c**.

Fig. 6 **a** Image quality map and **b** inverse pole figure with a confidence index value greater than 0.1 for the α' phase in the Ti-50 at% Hf alloy solution-treated at 1523 K followed by water quenching, respectively, as acquired using transmission electron microscopy-automated crystal lattice orientation mapping analysis. **c** Variant map and **d** area fraction of each CV based on the lattice correspondence, respectively. **e** Grain reference orientation deviation map corresponding to **c**.

Fig. 7 **a, d, f** Bright-field images of the Ti-50 at% Hf alloy solution-treated at 1323 K followed by water quenching. **b, c, e, g** Selected-area diffraction patterns corresponding to boundaries B and C in **a**, E in **d** and G in **f**, respectively.

Fig. 8 Schematic illustration of the orientation relationship between CV1(2) and **a** CV3(4), **b** CV5(6), **c** CV9(10), **d** CV11(12), **e** CV7(8), respectively.

Fig. 9 Schematic illustration of the formation process of martensite variants in the Ti-Hf alloy.

Table 1 Lattice parameters and reliability of the fitting results for the α and α' phase for the Ti-25 at% Hf and Ti-50 at% Hf alloys solution-treated at 1223 K and 1523 K, respectively, followed by furnace cooling and water quenching, which were refined using the Pawley method.

		a (nm)	*c* (nm)	R_{wp} (%)	S
Ti-25 at % Hf alloy	1223K_FC	0.303	0.478	4.36	4.16
	1223K_WQ	0.304	0.480	1.65	1.52
Ti-50 at % Hf alloy	1523K_FC	0.310	0.490	3.08	1.31
	1523K_WQ	0.311	0.490	1.54	1.48

Table 2 Lattice correspondence between the β parent phase and the α' martensite.

Correspondence variant	$(0001)_{\alpha'}$	$[11\bar{2}0]_{\alpha'}$
CV1	$(110)_{\beta}$	$[\bar{1}11]_{\beta}$
CV2	$(110)_{\beta}$	$[1\bar{1}1]_{\beta}$
CV3	$(011)_{\beta}$	$[1\bar{1}1]_{\beta}$
CV4	$(011)_{\beta}$	$[11\bar{1}]_{\beta}$
CV5	$(101)_{\beta}$	$[\bar{1}11]_{\beta}$
CV6	$(101)_{\beta}$	$[11\bar{1}]_{\beta}$
CV7	$(1\bar{1}0)_{\beta}$	$[111]_{\beta}$
CV8	$(1\bar{1}0)_{\beta}$	$[11\bar{1}]_{\beta}$
CV9	$(01\bar{1})_{\beta}$	$[111]_{\beta}$
CV10	$(01\bar{1})_{\beta}$	$[\bar{1}11]_{\beta}$
CV11	$(10\bar{1})_{\beta}$	$[111]_{\beta}$
CV12	$(10\bar{1})_{\beta}$	$[\bar{1}11]_{\beta}$

Table 3 Twinning shear of $\{10\bar{1}1\}_{\alpha'}$, $\{10\bar{1}2\}_{\alpha'}$ and $\{13\bar{4}1\}_{\alpha'}$ twins, based on the *c*/*a* ratio of the lattice parameters.

	$\{10\bar{1}1\}$	$\{10\bar{1}2\}$	$\{13\bar{4}1\}$
Ti-25 at% Hf alloy	0.0888	0.1854	0.6585
Ti-50 at% Hf alloy	0.0852	0.1897	0.6588

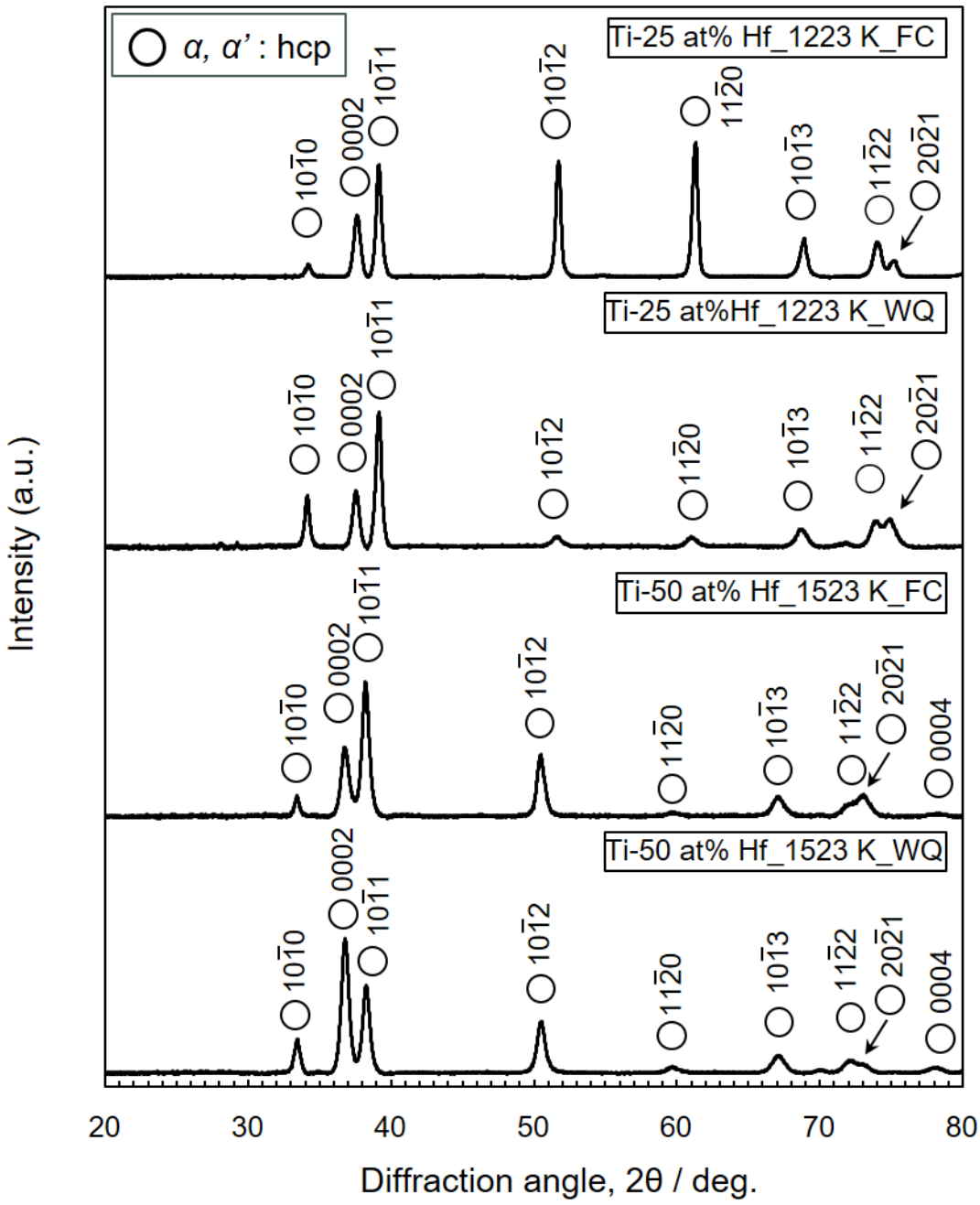

Fig. 1 Room-temperature XRD patterns of the Ti-25 at% Hf and Ti-50 at% Hf alloys solution-treated at 1223 K and 1523 K, respectively, followed by furnace cooling and water quenching.

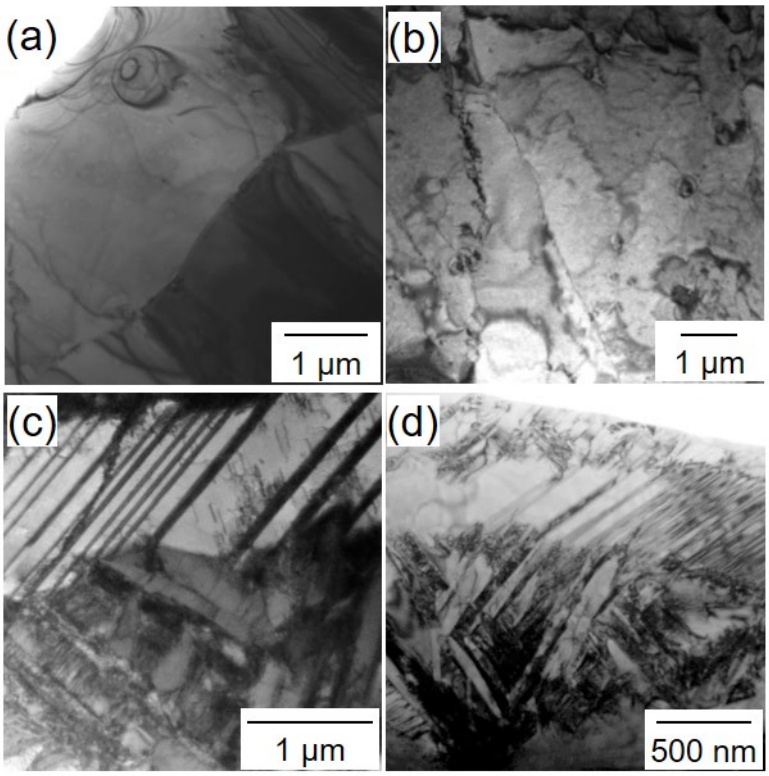

Fig. 2 **a, b** Bright-field images of the Ti-25 at% Hf and Ti-50 at% Hf alloys solution-treated at 1223 K and 1523 K, respectively, followed by furnace cooling. **c, d** Bright-field images of the Ti-25 at% Hf and Ti-50 at% Hf alloys solution-treated at 1223 K and 1523 K, respectively, followed by water quenching.

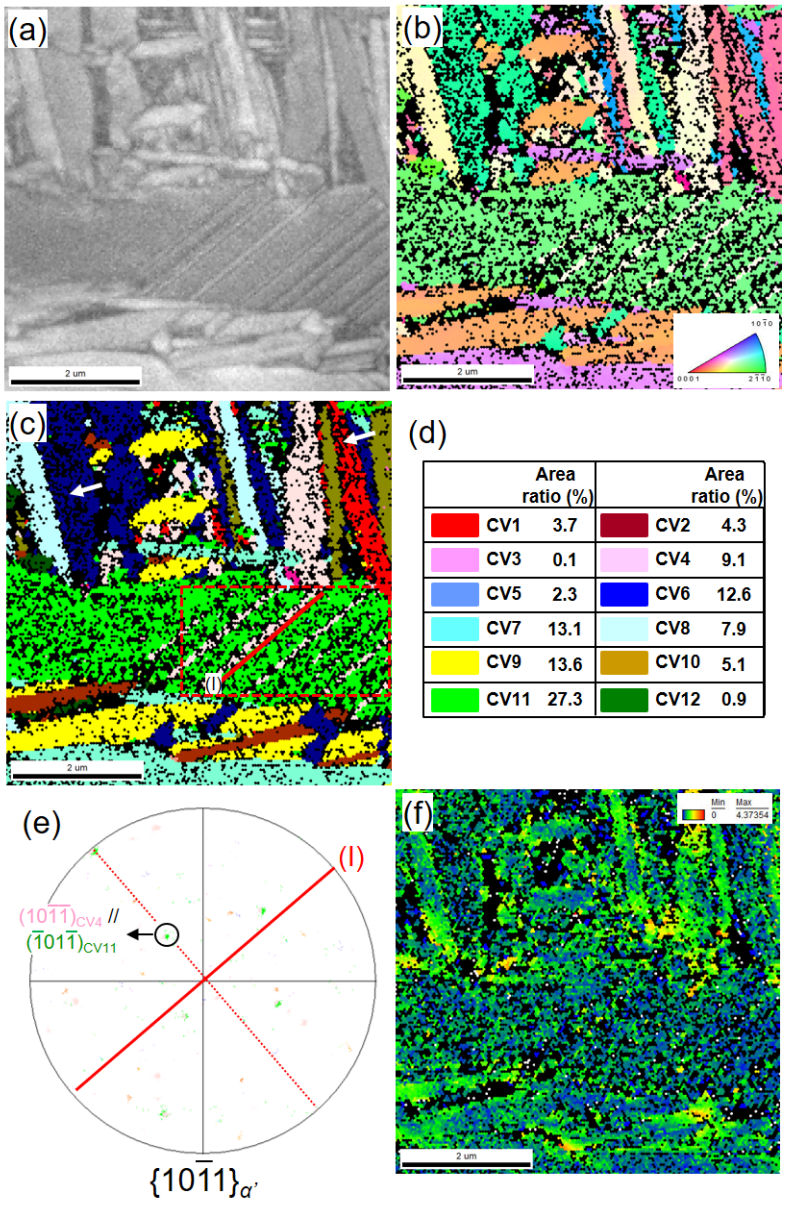

Fig. 3 **a** Image quality map and **b** inverse pole figure with a confidence index value greater than 0.1 for the α' phase in the Ti-25 at% Hf alloy solution-treated at 1123 K followed by water quenching, respectively, as obtained by transmission Kikuchi diffraction. **c** Variant map and **d** area fraction of each CV based on the lattice correspondence, respectively. **e** Pole figure recorded on the $\{10\bar{1}1\}_{\alpha'}$ plane in the red rectangular-shaped area in **c**. **f** Grain reference orientation deviation map corresponding to **c**.

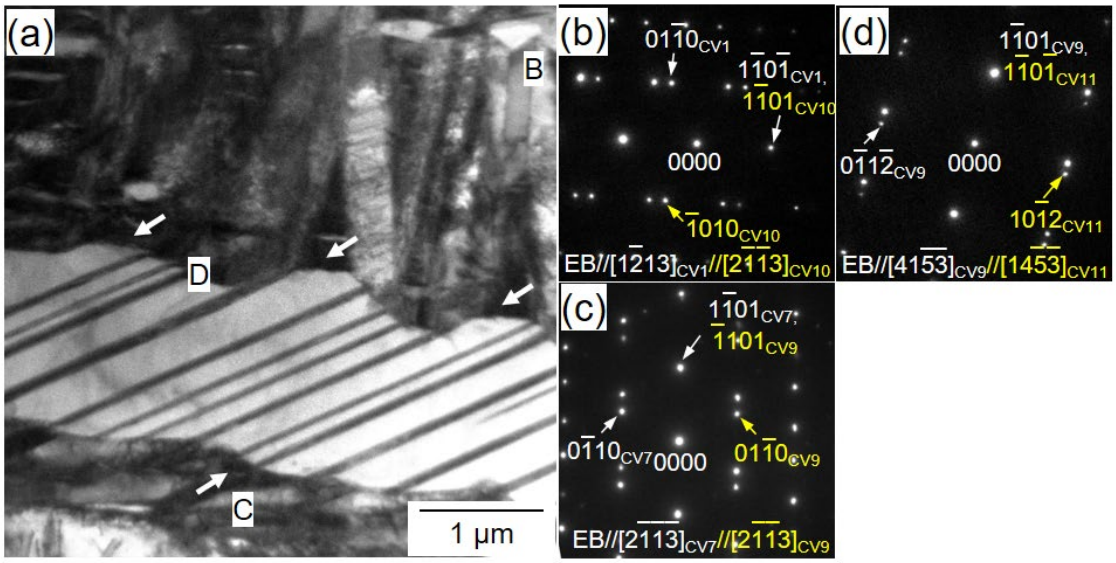

Fig. 4 **a** Bright-field image of the Ti-25 at% Hf alloy solution-treated at 1123 K followed by water quenching. **b, c, d** Selected-area diffraction patterns corresponding to boundaries B, C and D in **a**, respectively.

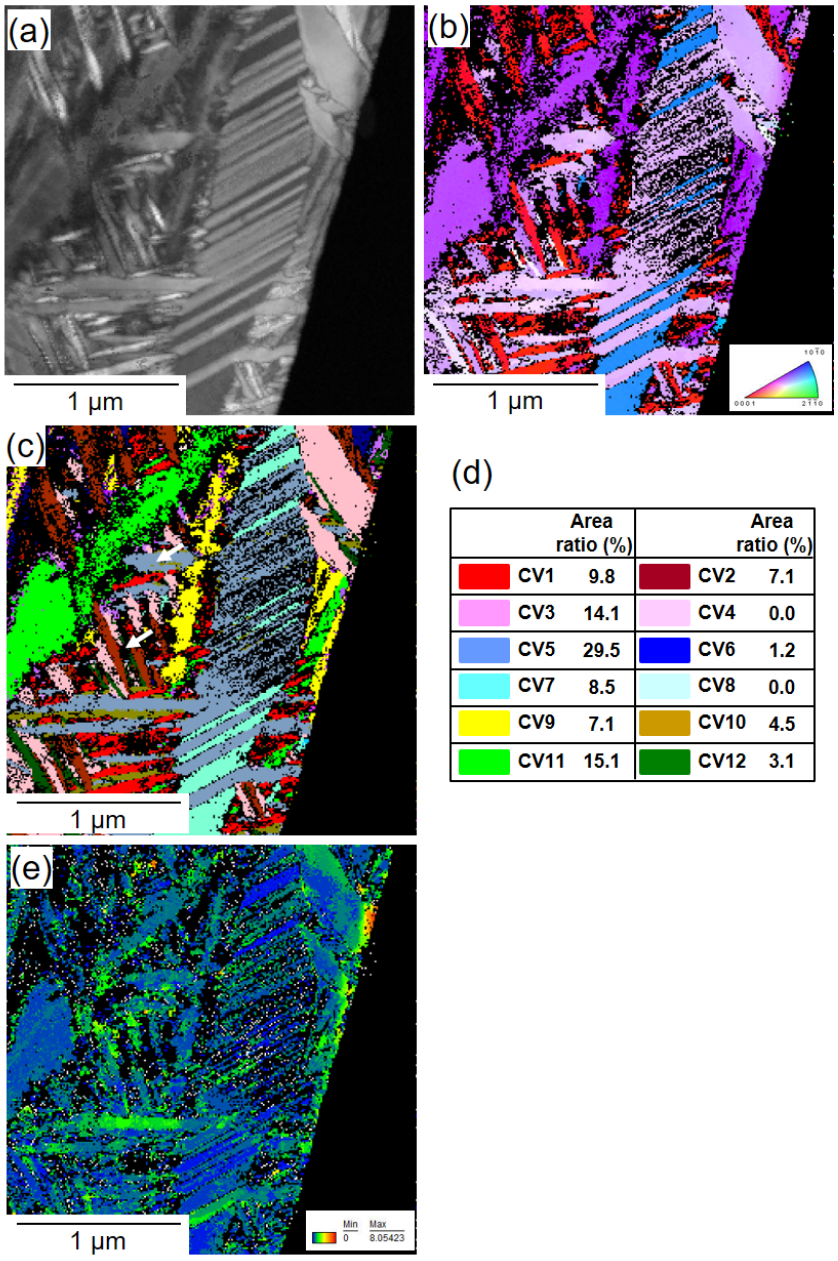

Fig. 5 **a** Image quality map and **b** inverse pole figure with a confidence index value greater than 0.1 for the α' phase in the Ti-50 at% Hf alloy solution-treated at 1523 K followed by water quenching, respectively, as acquired using transmission electron microscopy-automated crystal lattice orientation mapping analysis. **c** Variant map and **d** area fraction of each CV based on the lattice correspondence, respectively. **e** Grain reference orientation deviation map corresponding to **c**.

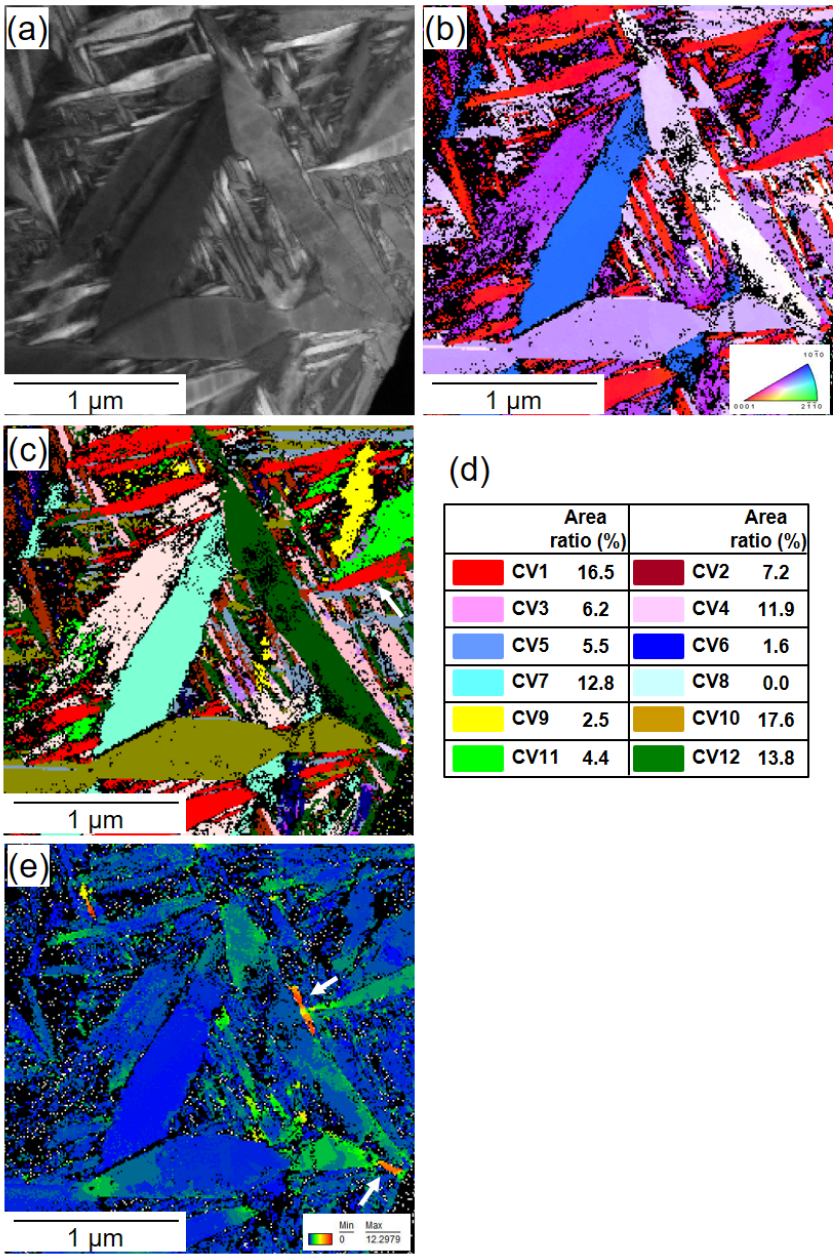

	Area ratio (%)		Area ratio (%)
CV1	16.5	CV2	7.2
CV3	6.2	CV4	11.9
CV5	5.5	CV6	1.6
CV7	12.8	CV8	0.0
CV9	2.5	CV10	17.6
CV11	4.4	CV12	13.8

Fig. 6 **a** Image quality map and **b** inverse pole figure with a confidence index value greater than 0.1 for the α' phase in the Ti-50 at% Hf alloy solution-treated at 1523 K followed by water quenching, respectively, as acquired using transmission electron microscopy-automated crystal lattice orientation mapping analysis. **c** Variant map and **d** area fraction of each CV based on the lattice correspondence, respectively. **e** Grain reference orientation deviation map corresponding to **c**.

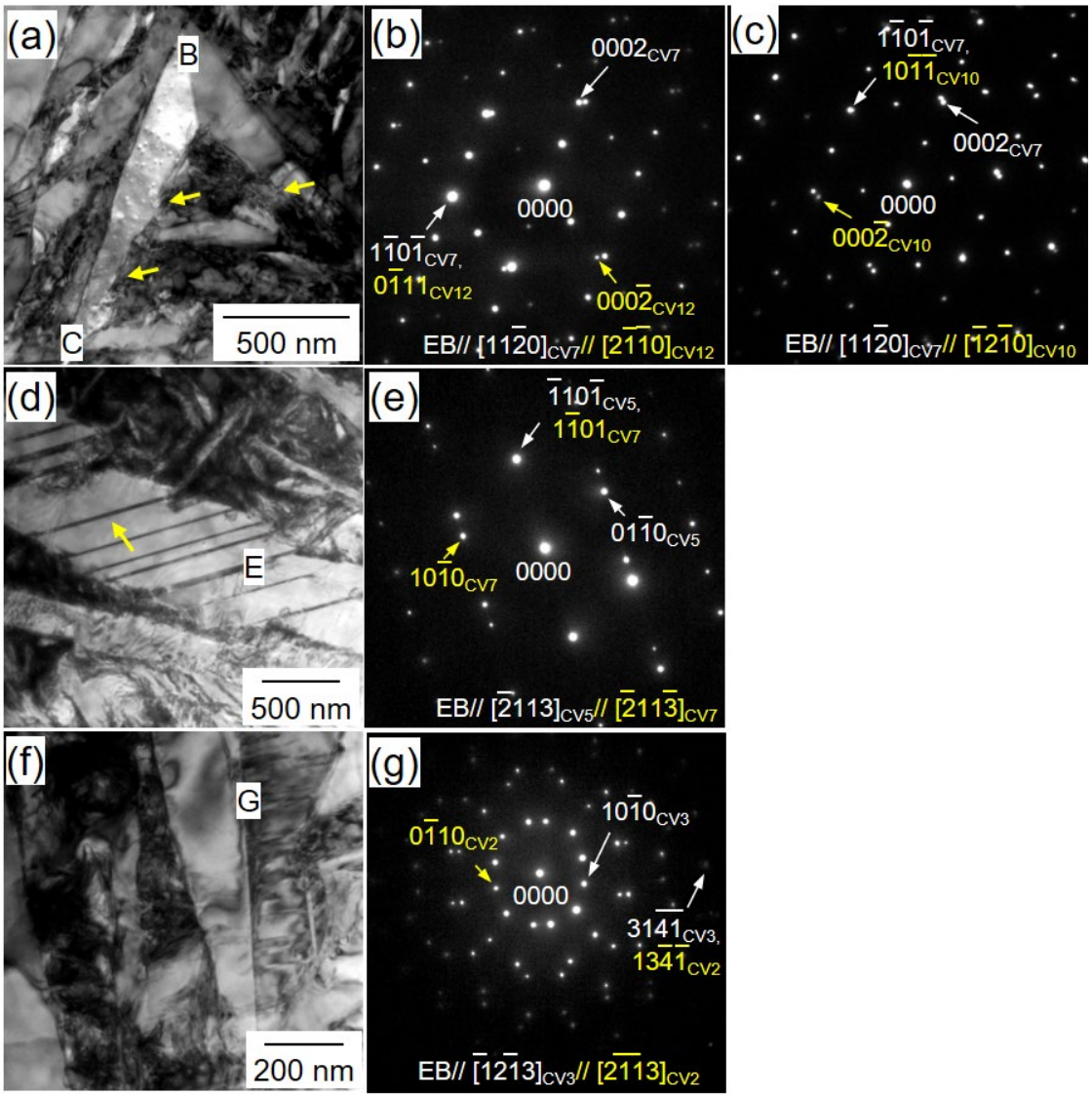

Fig. 7 **a, d, f** Bright-field images of the Ti-50 at% Hf alloy solution-treated at 1323 K followed by water quenching. **b, c, e, g** Selected-area diffraction patterns corresponding to boundaries B and C in **a**, E in **d** and G in **f**, respectively.

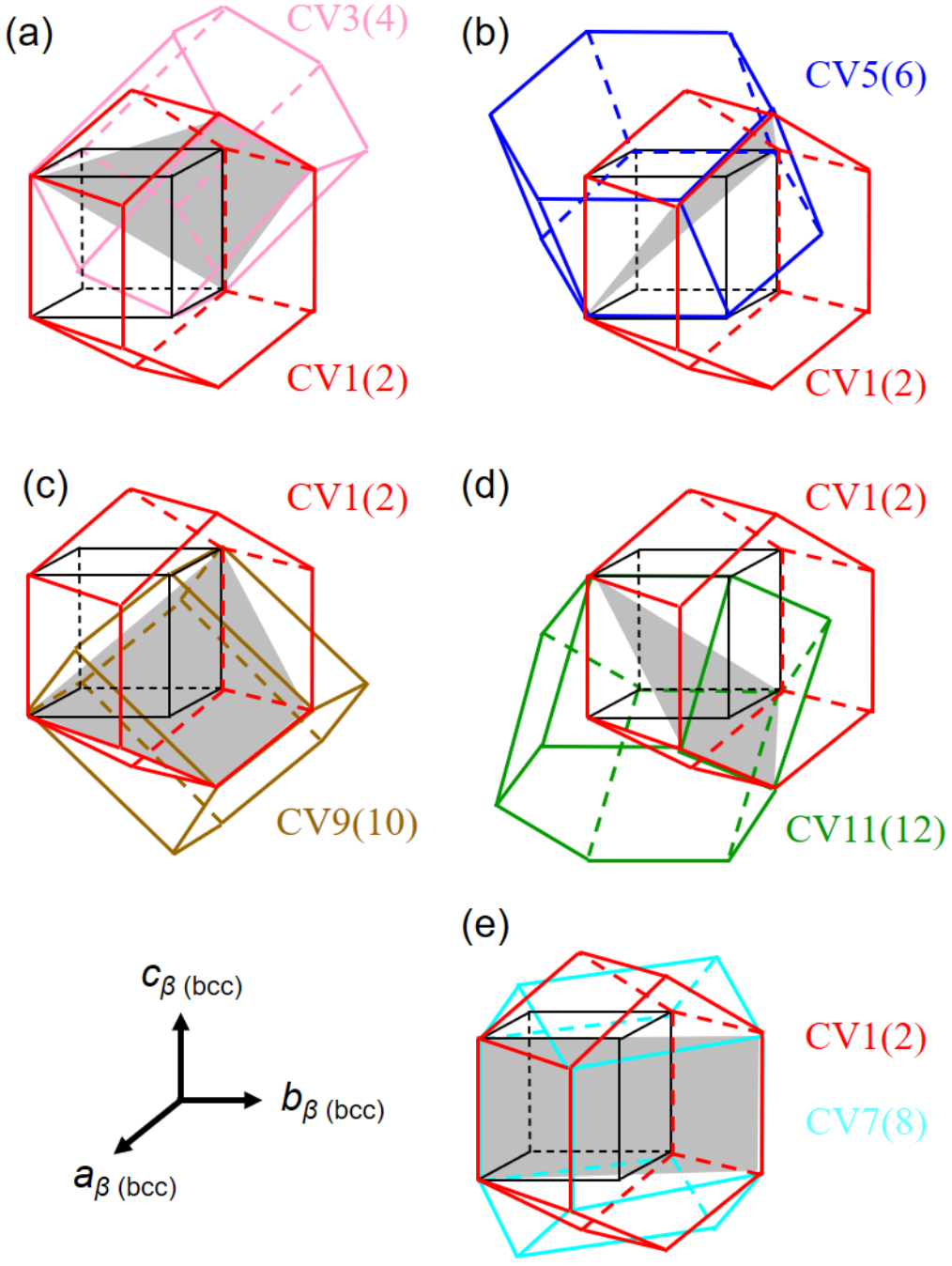

Fig. 8 Schematic illustration of the orientation relationship between CV1(2) and **a** CV3(4), **b** CV5(6), **c** CV9(10), **d** CV11(12), **e** CV7(8), respectively.

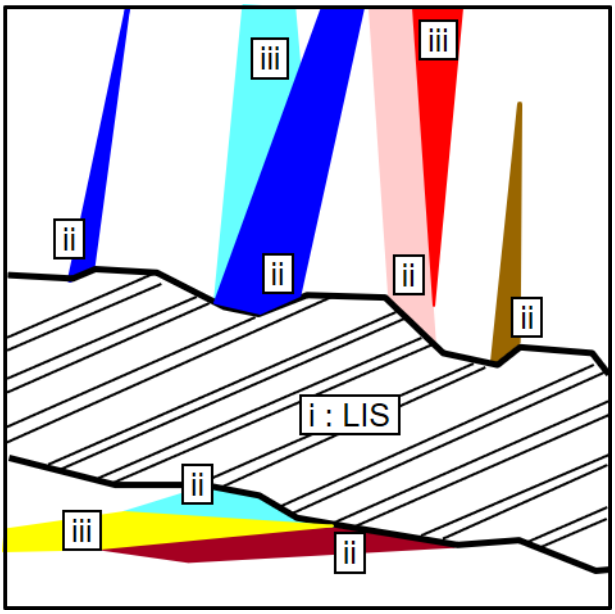

Fig. 9 Schematic illustration of the formation process of martensite variants in the Ti-Hf alloy.